Evolution of the hot flow of MAXI J1543-564

Rapisarda, S.; Ingram, A.; van der Klis, M.

Link to publication

Citation for published version (APA):
Rapisarda, S., Ingram, A., & van der Klis, M. (2014). Evolution of the hot flow of MAXI J1543-564. *Monthly Notices of the Royal Astronomical Society*, *440*(3), 2882-2893. https://doi.org/10.1093/mnras/stu461

Evolution of the hot flow of MAXI J1543-564

S. Rapisarda,[★] A. Ingram and M. van der Klis

Anton Pannekoek Institute for Astronomy, NL-1098 XH Amsterdam, the Netherlands

ABSTRACT

We present a spectral and timing analysis of the black hole (BH) candidate MAXI J1543-564 during its 2011 outburst. As shown in previous work, the source follows the standard evolution of a BH outburst. During the rising phase of the outburst, we detect an abrupt change in timing behaviour associated with the occurrence of a type-B quasi-periodic oscillation (QPO). This QPO and the simultaneously detected radio emission mark the transition between hard and soft intermediate state. We fit power spectra from the rising phase of the outburst using the recently proposed model PROPFLUC. This assumes a truncated disc/hot inner flow geometry, with mass accretion rate fluctuations propagating through a precessing inner flow. We link the PROPFLUC physical parameters to the phenomenological multi-Lorentzian fit parameters. The physical parameter dominating the QPO frequency is the truncation radius, while broad-band noise characteristics are also influenced by the radial surface density and emissivity profiles of the flow. In the outburst rise, we found that the truncation radius decreases from $r_o \sim 24$ to $10R_g$, and the surface density increases faster than the mass accretion rate, as previously reported for XTE J1550-564. Two soft intermediate state observations could not be fitted with PROPFLUC, and we suggest that they are coincident with the ejection of material from the inner regions of the flow in a jet or accretion of these regions into the BH horizon, explaining the drop in QPO frequency and suppression of broad-band variability preferentially at high-energy bands coincident with a radio flare.

Key words: accretion, accretion discs – X-rays: binaries – X-rays: individual: MAXI J1543-564.

1 INTRODUCTION

Transient black hole binaries (BHBs) display outbursts exhibiting several states, characterized by both spectral and timing properties (e.g. Belloni et al. 2005; Remillard & McClintock 2006; Belloni 2010; Gilfanov 2010). During the outburst, sources typically follow a 'q' shaped, anticlockwise track on a plot of X-ray flux versus spectral hardness ratio (hardness–intensity diagram: hereafter HID), with the quiescent state occupying the bottom-right corner. The initial transition from hard (LHS) to soft (HSS), via intermediate states, occurs when the power-law component of the spectrum is observed to soften (photon index $\Gamma \sim 1.7$–2.4) and a disc blackbody component (peaking in soft X-rays) becomes increasingly prominent. A power spectral analysis of the rapid variability reveals a quasi-periodic oscillation (QPO), which shows up as narrow harmonically related peaks, superimposed on broad-band continuum noise. The QPO fundamental frequency is observed to increase from ~0.1 to 10 Hz during the transition from the hard state, after which the X-ray emission becomes very stable in the soft state. Power spectral evolution correlates tightly with spectral evolution, with all the characteristic frequencies increasing with spectral hardness (e.g. Wijnands

& van der Klis 1998; Psaltis, Belloni & van der Klis 1999; Homan et al. 2001). QPOs observed coincident with broad-band noise are defined as type-C QPOs (Remillard et al. 2002; Casella, Belloni & Stella 2005). Type-B QPOs (Wijnands, Homan & van der Klis 1999), typically with a frequency of ~6–10 Hz, are observed in the intermediate state when the broad-band noise suddenly disappears. These features quickly evolve into type-A QPOs (Wijnands et al. 1999), which are broader and weaker. Since the sudden suppression of the broad-band noise hints a large physical change in the system, intermediate state observations displaying type-C QPOs are classified as hard intermediate state (HIMS) and those displaying type-A or B QPOs as soft intermediate state (SIMS). Additionally, a large radio flare, indicative of a jet ejection event, is often observed to be coincident with the onset of the SIMS (Fender, Belloni & Gallo 2004), although this is not always exact (Fender, Belloni & Gallo 2005).

The spectral and timing properties of BHBs can be described by *the truncated disc model*, (e.g. Esin, McClintock & Narayan 1997; Done, Gierliński & Kubota 2007) where an optically thick, geometrically thin accretion disc which produces the multitemperature blackbody spectral component (Shakura & Sunyaev 1973) truncates at some radius, r_o, larger than the innermost stable circular orbit (ISCO). In the region between this truncation radius r_o and

★ E-mail: S.N.Rapisarda@uva.nl

an inner radius r_i ($r_o > r_i > r_{ISCO}$), accretion takes place via a hot, optically thin, geometrically thick accretion flow (hereafter inner flow). Compton up-scattering of cool disc photons by hot electrons in the flow produces the power-law spectral component (Thorne & Price 1975; Sunyaev & Truemper 1979). In the hard state, r_o is large ($\sim 60 R_g$, where $R_g = GM/c^2$ is a gravitational radius), so only a small fraction of the disc photons illuminates the flow, giving rise to a weak direct disc component and hard power-law emission. As the average mass accretion rate increases during the outburst, r_o decreases, so more direct disc emission is seen and a greater luminosity of disc photons cool the flow, resulting in softer power-law emission. When r_o reaches the ISCO, the direct disc emission completely dominates the spectrum, and the transition to the soft state is complete.

This scenario is the framework of the propagating fluctuations model PROPFLUC (Ingram & Done 2011, 2012, hereafter ID11, ID12; Ingram & Van der Klis 2013, hereafter IK13), a model that can reproduce power density spectra by combining the effects of the propagation of mass accretion rate fluctuations in the inner flow (Lyubarskii 1997; Arévalo & Uttley 2006), responsible for generating the broad-band noise, with solid-body Lense–Thirring (LT) precession of this flow (Fragile et al. 2007; Ingram, Done & Fragile 2009), producing QPOs. Mass accretion rate fluctuations are generated throughout the inner flow, with the contribution to the rms variability from each region peaking at the local viscous frequency (e.g. Lyubarskii 1997; Churazov, Gilfanov & Revnivtsev 2001; Arévalo & Uttley 2006), thus the fast variability originates from the inner regions and the slow variability from the outer regions. As material is accreted, fluctuations propagate inwards, modulating the faster variability generated in the inner regions. Emission is thus highly correlated from all regions of the flow, giving rise to the observed linear rms–flux relation (Uttley & McHardy 2001; Uttley, McHardy & Vaughan 2005).

In this paper, we present a spectral and timing analysis of the source MAXI J1543-564 during its 2011 outburst. The source, discovered by MAXI/GSC (the Gas Slit Camera of the Monitor of ALL-sky X-ray Image; Matsuoka et al. 2009) on 2011 May 08 (Negoro et al. 2011), was first analysed by Stiele et al. (2012). Their analysis showed that the outburst evolution follows the usual BHBs behaviour, the exponential flux decay is interrupted by several flares, and during the transition from LHS and HSS, a type-C QPO is observed. Looking at other wavelengths, Miller-Jones et al. (2011) report the detection of radio emission at MJD 55695.73. In this work, we analyse the spectral and timing properties of the source in different energy bands, and we use the power density spectra of the rising phase of the outburst to systematically explore for the first time the capabilities of PROPFLUC.

2 OBSERVATIONS AND DATA ANALYSIS

We analysed data from the *RXTE* Proportional Counter Array (Jahoda et al. 1996) using 99 pointed observations collected between May 10 and 2011 September 30. Each observation consisted of between 300 and 4750 s of useful data.

We used Standard 2 mode data (16 s time resolution) to calculate a hard colour (HC) as the 16.0–20.0/2.0–6.0 keV count rate ratio and define the intensity as the count rate in the 2.0–20.0 keV band. All the observations were background subtracted, and all count rates were normalized by the corresponding Crab values closest in time to the observations.

We used the $\sim$125 μs time resolution Event mode and the $\sim$1 μs time resolution Good-Xenon mode data for Fourier timing

analysis. We constructed Leahy-normalized power spectra using 128 s data segments and 1/8192 s time bins to obtain a frequency resolution of 1/128 Hz and a Nyquist frequency of 4096 Hz. After averaging these power spectra per observation, we subtracted the Poisson noise using the method developed by Klein-Wolt (2004), based on the expression of Zhang et al. (1995), and renormalized the spectra to power density P_ν in units of (rms/mean)^2 Hz^{-1}. In this normalization, the fractional rms of a variability component is directly proportional to the square root of its integrated power density: rms $= 100\sqrt{\int_0^\infty P_\nu \mathrm{d}\nu}$ per cent. No background or dead-time corrections were made in computing the power spectra. This procedure was performed in four different energy bands: 2.87–4.90 keV (band 1), 4.90–9.81 keV (band 2), 9.81–20.20 keV (band 3), and the full 2.87–20.20 keV (band 0). The power spectra were fitted using a multi-Lorentzian function in which each Lorentzian contributing to the fit function is specified by a characteristic frequency $\nu_{max} = \sqrt{\nu_0^2 + (FWHM/2)^2}$ (Belloni, Psaltis & van der Klis 2002), and a quality factor $Q = \nu_0/FWHM$, where FWHM is the full width at half-maximum and ν_0 is the centroid frequency of the Lorentzian. All the power spectra shown in this paper were plotted using the power times frequency representation (νP_ν), in order to visualize ν_{max} as the frequency where the Lorentzian maximum occurs.

3 RESULTS

3.1 Light curve

The light curve of the source is shown in Fig. 1(a), where the 2–20 keV intensity is plotted versus time (MJD) for each pointed observation.

We subdivided the evolution of the outburst in five parts. In the first part of the outburst (MJD 556 91–556 96), the source rises to maximum intensity ($\sim$68 mCrab) in 5 d from the beginning of the *RXTE* observations. The second part (first grey area, MJD 556 96–557 13) is characterized by an intensity decay that is not smooth, but interrupted by four additional peaks with intensities between $\sim$47 and $\sim$58 mCrab. The third part (MJD 557 13–557 25, between the two grey areas) does not show any intensity peak but only a gradual decay. The following period (MJD 557 25–557 44, second grey area) is characterized by a broad maximum and several additional intensity peaks (between $\sim$34 and $\sim$42 mCrab) less luminous compared to those of the first grey area. Finally, the last part (MJD 557 44–558 34) consists of a relatively smooth decay until the end of the observations.

3.2 Color diagrams

Fig. 2 shows the HID, where the average intensity of each observation is plotted versus the HC. The source follows a counterclockwise path, starting and ending in the right (hard) part of the diagram at different luminosities. This is the usual behaviour observed for BH outbursts.

In order to better follow the spectral evolution of the source along the outburst, we also plotted in Fig. 1(c) the HC versus time.

In the first observation, the source is harder than Crab (HC = 1.71) and in the following six observations softens continuously, while at the same time its intensity increases from $\sim$24 to $\sim$68 mCrab. For the remaining observations, the source remains in the soft part of the HID (HC $\leq$ 0.5) except for the very last observation, where it goes back to a colour harder than Crab (HC = 1.31 $\pm$ 0.16).
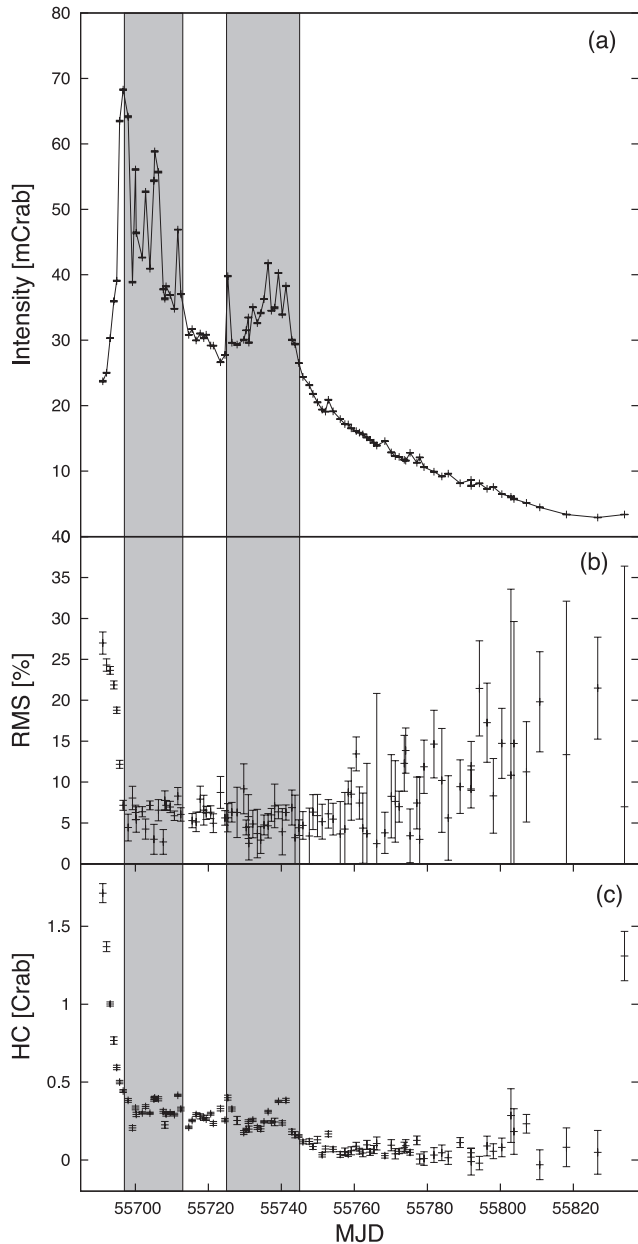
Figure 1. (a) Intensity [mCrab], (b) rms [per cent], (c) and HC [Crab] versus time for the 99 pointed observations. The grey rectangular areas indicate five time intervals characterized by different long-term luminosity variability. Data points are plotted with 1σ error bars.

As can be noted in Fig. 1(c), the transitions between hard and soft spectrum happen on short time-scales ($\sim$10 d) compared to the time spent by the source in the soft state ($\sim$125 d). However, while the initial transition from hard to soft state is simultaneous with a quick change in intensity ($+$188 per cent), the final transition (last observation) from soft to hard spectrum is characterized by a fractional intensity change of only $+$ 16 per cent, i.e. increasing when the source gets harder.

3.3 Time variability

The 1/129–10 Hz rms values as computed from the power spectra in band 0 are reported in Fig. 1(b). The first five observations, during which the source rapidly becomes softer and brighter are
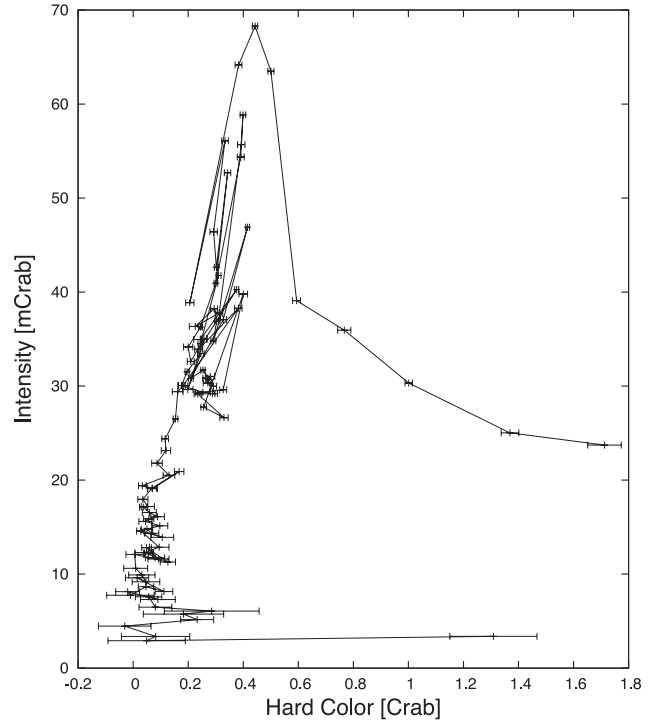
Figure 2. HC versus Intensity normalized to the Crab. Points represent average intensity and HC for each observation. 1σ error bars are plotted for the HC.

characterized by rms values of $\sim$19–27 per cent. In the remaining observations, the rms values are between $\sim$2 and $\sim$10 per cent with few exceptions.

Integrated rms is systematically higher for higher energies. From the beginning of the observations, as the intensity increases, integrated rms decreases independently from photon energy, but the rms decrease trend is different between energy bands. In order to better show these differences, we plotted in Fig. 3 the total fractional rms of the first seven observations for all the energy bands. Band 1 (red) shows a smooth and continuous rms decrease with time, while in band 2 (green) and band 3 (blue), the rms decrease is characterized by a 'jump' between observations 5 and 6 (Δrms ~-9 per cent in band 2, Δrms ~-11 per cent in band 3). Observation 6 is also characterized by the detection of radio emission, indicated by the orange arrow.

3.3.1 QPOs and broad-band features

Only in the first seven observations, we detect QPOs ($Q > 2$) and/or broad-band components ($Q < 2$) in at least some energy bands. We used the power spectrum of the fifth observation in band 0 (MJD 556 94.884, Fig. 4) as a reference to identify four significant ($\sigma > 3$, single-trial) components: a main QPO L_{LF}, its harmonic L_{LF}^+, a broad-band noise component L_b, and another broad-band component L_b^- at lower frequency. In our analysis, we reported all components with single trial significance $\sigma \geq 3$ and additionally those components with significance between 2σ and 3σ that could be identified as L_{LF}, L_{LF}^+, L_b, or L_b^-. Table 1 shows ν, Q, rms, significance (σ) and reduced χ^2 for every fitted component in the seven observations analysed (1–7) for all the energy bands. We also report the 99.87 per cent upper limits calculated fixing ν and Q to values equal to the most significant corresponding component between the energy bands fitted in the same observation. Empty
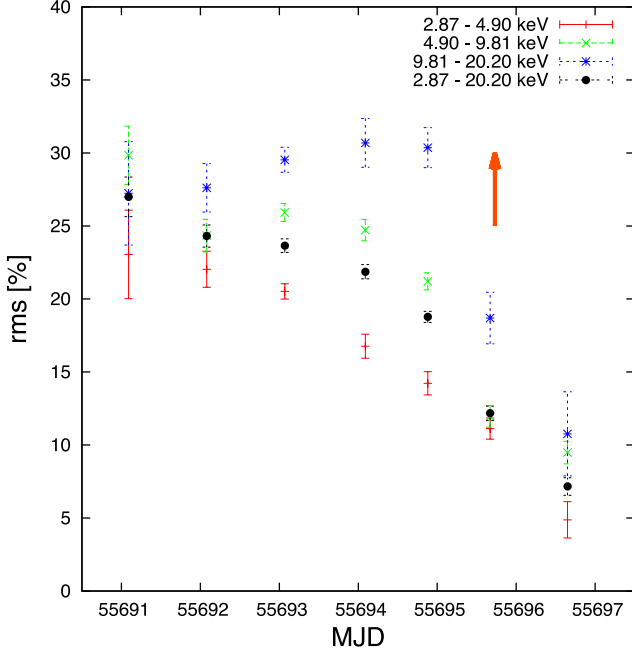
Figure 3. Fractional integrated 1/128–10 Hz rms versus time in the first seven observations for the bands considered. The orange arrow represents the time of the radio emission. All values are plotted with 1σ error bars.
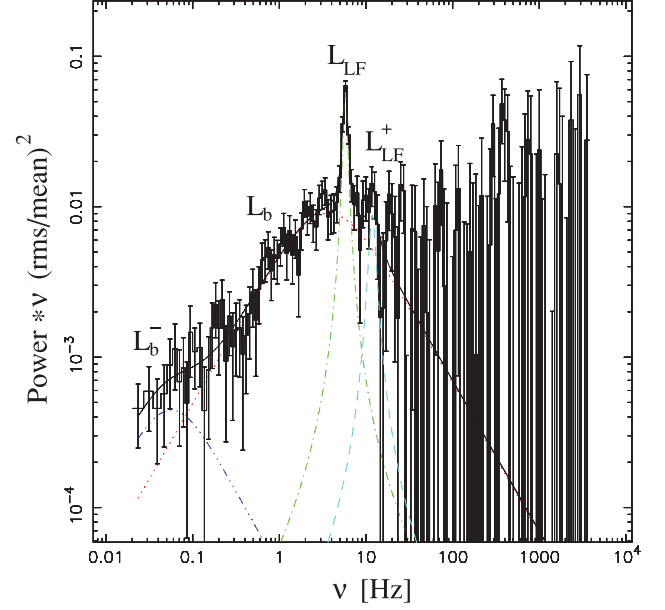

Figure 4. Multi-Lorentzian fit of the fifth power spectrum. Four main components were identified: a main QPO L_{LF}, its harmonic L_{LF}^+, a broad-band noise component L_b, and another broad component at lower frequency L_b^-.

Table 1. Multi-Lorentzian best-fitting parameters for observations 1–7 in four different energy bands.

Date (MJD)	Power spectrum component	Energy band (keV)	ν (Hz)	Q	rms (%)	σ	χ^2_{red}
		2.87–4.90	$1.07^{+0.04}_{-0.05}$	$4.17^{+2.07}_{-1.01}$	$17.97^{+1.85}_{-1.85}$	4.86	1.03
		4.90–9.81	$1.03^{+0.03}_{-0.02}$	$3.42^{+1.10}_{-0.84}$	$20.80^{+1.57}_{-1.64}$	6.36	1.07
556 91.089(1)	L_{LF}	9.81–20.20	$1.04^{+0.02}_{-0.02}$	$8.38^{+2.55}_{-2.55}$	$17.42^{+2.07}_{-2.07}$	4.21	0.81
		2.87–20.20	$1.06^{+0.02}_{-0.02}$	$5.26^{+1.34}_{-1.05}$	$17.48^{+1.27}_{-1.24}$	7.05	0.88
		2.87–4.90	$1.72^{+0.02}_{-0.03}$	$6.54^{+3.07}_{-1.64}$	$13.37^{+1.11}_{-1.06}$	6.32	1.17
		4.90–9.81	$1.75^{+0.02}_{-0.01}$	$10.91^{+7.32}_{-2.63}$	$14.34^{+0.92}_{-0.89}$	8.04	0.87
556 92.084(2)	L_{LF}	9.81–20.20	$1.74^{+0.02}_{-0.02}$	$6.46^{+2.68}_{-1.48}$	$18.69^{+1.57}_{-1.47}$	6.35	0.83
		2.87–20.20	$1.75^{+0.01}_{-0.01}$	$7.81^{+1.55}_{-1.15}$	$14.74^{+0.67}_{-0.66}$	11.17	0.91
		2.87–4.90	$2.97^{+0.02}_{-0.02}$	$7.82^{+1.61}_{-1.14}$	$11.25^{+0.57}_{-0.54}$	10.49	1.04
		4.90–9.81	$2.97^{+0.01}_{-0.01}$	$9.51^{+1.28}_{-0.98}$	$16.06^{+0.43}_{-0.43}$	18.93	1.04
556 93.066(3)	L_{LF}	9.81–20.20	$2.97^{+0.01}_{-0.02}$	$11.06^{+4.25}_{-2.07}$	$16.37^{+0.72}_{-0.67}$	12.18	0.88
		2.87–20.20	$2.97^{+0.01}_{-0.01}$	$8.60^{+0.69}_{-0.60}$	$14.60^{+0.29}_{-0.29}$	25.14	1.22
		2.87–4.90	$4.39^{+0.03}_{-0.07}$	$12.35^{+5.33}_{-5.33}$	$8.37^{+1.06}_{-0.86}$	4.86	0.84
		4.90–9.81	$4.42^{+0.05}_{-0.05}$	$9.18^{+1.44}_{-1.15}$	$14.57^{+1.00}_{-1.00}$	7.30	0.89
556 94.095(4)	L_{LF}	9.81–20.20	$4.46^{+0.07}_{-0.05}$	$7.00^{+1.57}_{-1.10}$	$19.62^{+1.55}_{-1.60}$	6.14	1.00
		2.87–20.20	$4.381^{+0.02}_{-0.02}$	$11.27^{+3.19}_{-1.87}$	$13.01^{+0.51}_{-0.49}$	13.18	0.91
		2.87–4.90	$5.67^{+0.15}_{-0.14}$	$6.61^{+9.13}_{-2.64}$	$7.35^{+1.65}_{-1.26}$	2.93	1.04
		4.90–9.81	$5.84^{+0.10}_{-0.11}$	$8.48^{+2.52}_{-1.32}$	$11.10^{+1.04}_{-1.01}$	5.50	1.07
556 94.884(5)	L_{LF}	9.81–20.20	$5.83^{+0.11}_{-0.12}$	$6,52^{+2.95}_{-1.83}$	$17.41^{+2.66}_{-2.44}$	3.57	0.91
		2.87–20.20	$5.77^{+0.05}_{-0.05}$	$7.98^{+1.20}_{-0.93}$	$10.43^{+0.61}_{-0.61}$	8.53	0.80
		2.87–4.90	$6.52^{+0.42}_{-0.76}$	$3.69^{+7.40}_{-1.87}$	$5.51^{+1.64}_{-1.26}$	2.19	1.10
		4.90–9.81	$5.74^{+0.22}_{-0.22}$	$4.96^{+4.99}_{-2.37}$	$6.08^{+1.42}_{-1.12}$	2.15	1.08
556 95.669(6)	L_{LF}	9.81–20.20	$6.19^{+0.27}_{-0.36}$	$4.45^{+8.57}_{-2.31}$	$12.84^{+2.87}_{-2.67}$	2.40	1.08
		2.87–20.20	$5.75^{+0.41}_{-0.49}$	$1.81^{+1.18}_{-0.86}$	$6.35^{+2.05}_{-1.28}$	2.49	1.08
		2.87–4.90	4.69	9.00	< 5.32	–	–
		4.90–9.81	$4.83^{+0.10}_{-0.06}$	$10.38^{+4.50}_{-4.60}$	$5.34^{+0.91}_{-0.67}$	3.97	0.84

Table 1. – *continued*

Date (MJD)	Power spectrum component	Energy band (keV)	ν (Hz)	Q	rms (%)	σ	$\chi^2_{\rm red}$
556 96.650(7)	$L_{\rm LF}$	9.81–20.20	$4.86^{+0.06}_{-0.17}$	$10.49^{+4.62}_{-4.62}$	$11.37^{+1.59}_{-1.42}$	4.00	1.21
		2.87–20.20	$4.69^{+0.05}_{-0.04}$	9.00	$4.76^{+0.36}_{-0.37}$	6.48	1.01
		2.87–4.90	2.28	4.55	< 6.48	–	–
		4.90–9.81	$2.28^{+0.56}_{-0.09}$	$4.55^{+5.92}_{-3.71}$	$13.05^{+7.56}_{-2.57}$	2.53	1.07
556 91.089(1)	$L_{\rm LF}^{+}$	9.81–20.20	$2.99^{+0.17}_{-0.14}$	4.55	< 22.34	$14.73^{+3.19}_{-3.19}$	0.81
		2.87–20.20	$2.17^{+0.15}_{-0.14}$	6.78	$5.42^{+2.10}_{-2.12}$	1.29	0.88
		2.87–4.90	$4.03^{+0.21}_{-0.13}$	$5.18^{+4.74}_{-2.32}$	$10.31^{+2.34}_{-1.86}$	2.78	1.17
		4.90–9.81	4.03	5.18	< 12.69	–	–
556 92.084(2)	$L_{\rm LF}^{+}$	9.81–20.20	–	–	–	–	
		2.87–20.20	4.03	5.18	< 8.00	–	–
		2.87–4.90	$5.87^{+0.16}_{-0.15}$	$5.18^{+4.74}_{-2.32}$	$6.24^{+1.27}_{-1.25}$	2.50	1.04
		4.90–9.81	$5.87^{+0.16}_{-0.15}$	$7.29^{+1.88}_{-1.88}$	$6.57^{+1.15}_{-1.02}$	3.23	1.04
556 93.066(3)	$L_{\rm LF}^{+}$	9.81–20.20	–	–	–	–	–
		2.87–20.20	$5.85^{+0.11}_{-0.11}$	$6.55^{+2.89}_{-1.53}$	$6.16^{+0.83}_{-0.73}$	4.23	1.22
		2.87–4.90	8.86	6.69	< 9.50	–	–
		4.90–9.81	8.86	5.88	$6.87^{+3.06}_{-2.21}$	1.55	0.89
556 94.095(4)	$L_{\rm LF}^{+}$	9.81–20.20	–	–	–	–	–
		2.87–20.20	$8.86^{+0.26}_{-0.28}$	$6.69^{+3.02}_{-3.02}$	$5.88^{+1.60}_{-1.16}$	2.55	0.91
		2.87–4.90	–	–	–	–	–
		4.90–9.81	3.30	0	< 30.16	–	–
556 91.089(1)	$L_{\rm b}$	9.81–20.20	–	–	–	–	–
		2.87–20.20	$3.30^{+1.33}_{-0.87}$	0	$19.55^{+2.37}_{-2.32}$	4.22	0.88
		2.87–4.90	–	–	–	–	–
		4.90–9.81	$3.641^{+0.86}_{-0.67}$	0	$22.12^{+1.71}_{-1.67}$	6.64	0.87
556 92.084(2)	$L_{\rm b}$	9.81–20.20	$7.881^{+7.40}_{-3.33}$	0	$24.65^{+4.60}_{-3.73}$	3.31	0.83
		2.87–20.20	$3.61^{+0.41}_{-0.36}$	0	$21.38^{+0.89}_{-0.89}$	11.96	0.91
		2.87–4.90	$4.813^{+0.74}_{-0.69}$	0	$18.71^{+1.42}_{-1.21}$	7.72	1.04
		4.90–9.81	$3.755^{+0.52}_{-0.50}$	0	$21.25^{+1.25}_{-1.27}$	8.38	1.04
556 93.066(3)	$L_{\rm b}$	9.81–20.20	$4.261^{+0.66}_{-0.63}$	0	$27.40^{+1.67}_{-1.69}$	8.09	0.88
		2.87–20.20	$3.77^{+0.27}_{-0.27}$	0	$19.98^{+0.61}_{-0.63}$	15.83	1.22
		2.87–4.90	$4.64^{+0.74}_{-0.69}$	0	$15.14^{+1.74}_{-1.69}$	4.48	0.83
		4.90–9.81	$3.44^{+0.78}_{-0.69}$	0	$20.28^{+1.78}_{-1.68}$	6.02	0.89
556 94.095(4)	$L_{\rm b}$	9.81–20.20	$1.71^{+0.84}_{-0.49}$	0	$21.61^{+3.04}_{-2.47}$	4.38	1.00
		2.87–20.20	$3.42^{+0.52}_{-0.49}$	0	$18.19^{+1.70}_{-1.05}$	8.69	0.91
		2.87–4.90	$5.36^{+2.01}_{-1.63}$	0	$13.18^{+1.92}_{-1.87}$	3.52	1.04
		4.90–9.81	$4.36^{+0.80}_{-0.72}$	0	$20.28^{+1.28}_{-1.24}$	8.11	1.07
556 94.884(5)	$L_{\rm b}$	9.81–20.20	$3.54^{+1.34}_{-0.98}$	0	$25.89^{+3.45}_{-2.95}$	4.39	0.91
		2.87–20.20	$3.69^{+0.67}_{-0.57}$	0	$16.90^{+0.99}_{-0.93}$	8.53	0.80
		2.87–4.90	–	–	–	–	–
		4.90–9.81	$2.50^{+0.23}_{-0.22}$	$1.69^{+0.89}_{-0.70}$	$6.94^{+1.17}_{-1.00}$	3.48	1.08
556 95.669(6)	$L_{\rm b}$	9.81–20.20	–	–	–	–	–
		2.87–20.20	$3.08^{+1.04}_{-0.91}$	0	$8.56^{+1.42}_{-1.38}$	3.10	1.08
		2.87–4.90	1.55	0	< 5.03	–	–
		4.90–9.81	$1.55^{+0.94}_{-0.56}$	0	$6.68^{+1.25}_{-1.01}$	3.32	0.84
556 96.650(7)	$L_{\rm b}$	9.81–20.20	–	–	–	–	–
		2.87–20.20	–	–	–	–	–
		2.87–4.90	$0.06^{+0.05}_{-0.03}$	0	$3.27^{+0.84}_{-0.76}$	2.15	1.04
		4.90–9.81	0.06	0.13	< 5.07	–	–
556 94.884(5)	$L_{\rm b}^{-}$	9.81–20.20	–	–	–	–	–
		2.87–20.20	$0.057^{+0.05}_{-0.02}$	$0.13^{+0.48}_{-0.48}$	$3.54^{+0.90}_{-0.58}$	3.04	0.80
		2.87–4.90	$0.19^{+0.06}_{-0.05}$	0	$4.76^{+0.56}_{-0.53}$	4.49	1.10
		4.90–9.81	$0.26^{+0.76}_{-0.11}$	0	$4.62^{+0.92}_{-0.81}$	2.86	1.08

Table 1. – *continued*

Date (MJD)	Power spectrum component	Energy band (keV)	ν (Hz)	Q	rms (%)	σ	χ^2_{red}
556 95.669(6)	L_{b}^-	9.81–20.20	$0.52^{+2.04}_{-0.26}$	0	$10.47^{+6.41}_{-1.98}$	2.64	1.08
		2.87–20.20	$0.13^{+0.04}_{-0.03}$	0	$4.42^{+0.47}_{-0.44}$	5.00	1.08
		2.87–4.90	–	–	–	–	–
		4.90–9.81	–	–	–	–	–
556 96.650(7)	L_{b}^-	9.81–20.20	–	–	–	–	–
		2.87–20.20	$0.27^{+0.39}_{-0.15}$	0	$2.49^{+0.79}_{-0.56}$	2.23	0.91
556 92.084(2)	?	2.87–4.90	$0.561^{+0.01}_{-0.04}$	$6.88^{+18.05}_{-3.11}$	$6.65^{+1.17}_{-0.97}$	3.42	1.10
			$2.74^{+0.06}_{-0.09}$	$6.10^{+11.11}_{-2.33}$	$10.28^{+1.94}_{-1.63}$	3.16	1.10
556 95.669(6)	L_{LF} sub?	2.87–4.90	$3.38^{+0.27}_{-0.22}$	$2.40^{+1.61}_{-0.89}$	$6.57^{+1.21}_{-1.15}$	2.85	1.10
		2.87–20.20	$3.11^{+0.12}_{-0.09}$	$6.33^{+3.45}_{-3.45}$	$3.67^{+1.42}_{-0.83}$	2.20	1.10
556 96.650(7)	L_{LF} sub?	2.87–20.20	$2.43^{+0.06}_{-0.04}$	9.00	$2.79^{+0.44}_{-0.49}$	2.85	1.01
	L_{b} ?	2.87–20.20	$1.57^{+0.19}_{-0.12}$	$3.27^{+4.16}_{-1.63}$	$2.70^{+0.78}_{-0.64}$	2.23	1.01

lines mean that no components were fitted and no upper limit could be determined.

Figs 5(g) and (h) show the frequencies of the fitted QPOs (triangles for L_{LF}, diamonds for L_{LF}^+), broad-band components (squares for L_{b}, circles for L_{b}^-),** and unidentified narrow ($Q > 2$) components (pentagons), and their rms versus time in band 0, respectively. Solid symbols indicate significant components and open symbols components with significance between 2σ and 3σ. The 2–3σ unidentified component of observation 6 (see Table 1, bottom) is included in our plot because its characteristic frequency matches with the subharmonic frequency of the identified component L_{LF}. Similarly, two 2–3σ unidentified components fitted in observation 7 (Fig. 6) were reported, as one matches with the subharmonic frequency of L_{LF}, and the other with L_{b}. Squares and circles were slightly shifted to the right for clarity.

Always referring to band 0, in the first five observations one significant low-frequency QPO (L_{LF}) was fitted for each spectrum and only the third observation shows a significant harmonic (L_{LF}^+). The L_{LF} frequency increases with time from $\sim$1.1 to $\sim$5.8 Hz while its rms decreases from $\sim$17 to $\sim$10 per cent (see Table 1). Observation 7 shows a significant QPO with $\nu_{\mathrm{max}} = 4.7$ Hz (Fig. 6). The peak characteristics ($\nu_{\mathrm{max}} = 4.7$ Hz, $Q = 9$, rms $\sim$4.8) of and the low 1/128–10 Hz rms ($\sim$7.2 per cent) associated with this QPO, are characteristics of type-B QPOs (e.g. Casella et al. 2005). Considering also the 2–3σ QPO fitted in observation 6 ($\nu_{\mathrm{max}} = 5.7$ Hz, $\sigma \sim 2.5$), in observations 6 and 7 L_{LF} frequency and rms are not anticorrelated anymore. The characteristic frequency of L_{LF} decreases from $\sim$5.8 to $\sim$4.7 Hz while the rms still decreases from $\sim$6 to $\sim$5 per cent.

One significant broad-band component (L_{b}) with ν_{max} in the interval $\sim$2–4 Hz was fitted in observations 1–6. The rms of this component decreases with time (from 20 to 9 per cent), with a clear decreasing trend observable only in observations 5 and 6, while its ν_{max} remains almost in the same frequency range (around 3 Hz). In observations 5–7, we fitted another broad-band component (L_{b}^-) characterized by an increasing ν_{max} (from observation 5 to 7) in the interval $\sim$0.06–0.66 Hz and rms between 2 and 4 per cent.

The timing features in the other energy bands are reported in Figs 5(a)–(f). Similarly panels (g) and (h), plots (a) and (b), (e) and (d), and (e) and (f) show frequency and rms evolution for power spectral components fitted in bands 1, 2, and 3, respectively. No significant characteristic frequency shift was detected between energy bands in any power spectral component, while the rms values are systematically higher for higher energies (Table 1). In band 1, L_{LF} frequency increases with time (from $\sim$1.1 to $\sim$6.5 Hz) in the first six observations while no significant QPO was fitted in observation 7. The behaviour of L_{LF} characteristic frequency in bands 2 and 3 is mostly identical to band 1 for observations 1–5, but we observe some differences in observations 6 and 7. The 2–3σ QPO ($\sigma \sim 2.2$) fitted in observation 6 (band 2) seems to break the anticorrelation between frequency and rms shown in observations 1–5, but in band 3 the QPO frequency error bar is too big to infer any trend. However, the anticorrelation is evident in observation 7, where a significant QPO was fitted in bands 2 and 3 with lower characteristic frequency compared to observation 5. The rms of L_{LF} in band 1 decreases as the QPO frequency increases, but in bands 2 and 3 this trend is progressively weaker. Indeed, in band 3 the L_{LF} rms slightly oscillates around $\sim$17 and $\sim$11 per cent in the first five observations and decreases to $\sim$11 per cent only in the last two observations.

The broad-band component (L_{b}) frequency slightly varies around $\sim$5 Hz in observations 3–5 (band 1), while no significant broad-band components were fitted in observations 6 and 7. In band 2, L_{b} frequency shows a clear decreasing trend only in the last three observations ($\nu \sim 4.4$–1.6 Hz), while does not show any clear trend in band 3. L_{b} rms decreases smoothly with time in band 1 (from $\sim$22 to $\sim$15 per cent), but it does not show the same trend in the other two energy bands. In band 2, we observe a clear decrease of L_{b} rms only in observations 5–6 (from $\sim$20 to $\sim$7 per cent), and in band 3 it oscillates between 22 and 27 per cent.

Apart from the full energy, L_{b}^- was fitted only in observations 5 (band 1) and 6 (band 1–3), but it is significant just at low photon energy (band 1, 6). L_{b}^- frequency and rms behaviour in band 1 is mostly identical to band 0.

4 MODEL FITTING

We fit the power spectra of the first five observations using PROPFLUC (ID11; ID12; IK13). Whereas original explorations of the model (ID11; ID12) used computationally intensive Monte Carlo simulations, IK13 developed an exact analytic version of the model, allowing us for the first time to explore its capabilities systematically. We also investigate the relation between the values we obtained from the previously described phenomenological fitting of several Lorentzians (Sections 2 and 3) and the model physical
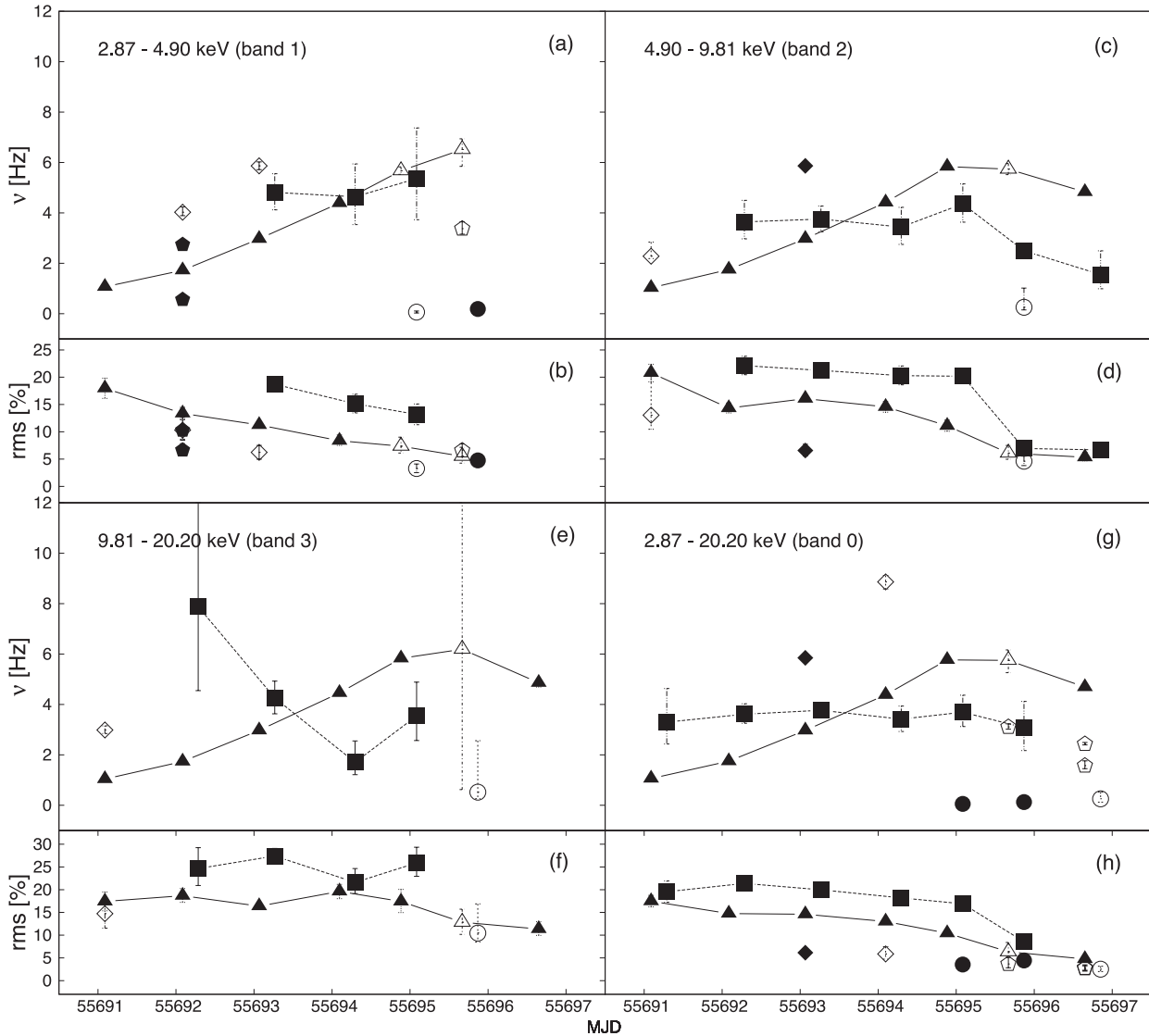
Figure 5. Characteristic frequency and rms of L_{LF} (triangles), L_{LF}^{+} (diamonds), L_b (squares), L_b^{-} (circles), and other significant unidentified components (pentagons) fitted in the first seven observations in all the energy bands (L_b and L_b^{-} have been shifted slightly to the right with respect to the original position for clear reading). Open symbols indicate components with significance between 2 and 3σ, while full symbols stand for $\sigma > 3$ significant components. All values are plotted with 1σ error bars.

parameters (see table 2 in ID12 for a summary and description of all the physical parameters).

4.1 The model

PROPFLUC (Section 1) parametrizes the flow surface density profile, which is required to calculate both the precession frequency and local viscous frequency, as a bending power law:[1]

$$\Sigma(r) = \frac{\Sigma_0 \dot{M}_0}{c R_g} \frac{x^\lambda}{(1 + x^\kappa)^{(\zeta + \lambda)/\kappa}}, \qquad (1)$$

where $x = r/r_{bw}$ and r_{bw} is a break radius such that $\Sigma(r) \sim r^{-\zeta}$ for $r \gg r_{bw}$ and $\Sigma(r) \sim r^{-\lambda}$ for $r \ll r_{bw}$, with the sharpness of the break controlled by the parameter κ (Fig. 7b shows $\Sigma(r)$ examples for

---

[1] ID12 showed that this surface density profile describes that measured from Fragile et al. (2007)'s simulations.

different r_{bw} values). Here, $\dot{M}_0$ is the average mass accretion rate over the course of a single observation, and Σ_0 is a dimensionless normalization constant. Throughout this paper, we employ the convention that $r \equiv R/R_g$ is radius expressed in units of R_g. The surface density drop off at the bending wave radius, r_{bw}, is due to the torque created by the radial dependence of LT precession ($\nu_{LT} \propto \sim r^{-3}$); i.e. essentially the inner regions try to precess quicker than the outer regions. Outside r_{bw}, bending waves (pressure waves) strongly couple the flow together but inside r_{bw}, material falls quickly towards the BH (Lubow, Ogilvie & Pringle 2002; Fragile et al. 2007). The precession frequency of the flow is given by (Liu & Melia 2002):

$$\nu_{prec} = \nu_{qpo} = \frac{\int_{r_i}^{r_o} f_{LT} f_k \Sigma(r) r^3 dr}{\int_{r_i}^{r_o} f_k \Sigma(r) r^3 dr}, \qquad (2)$$

where f_k is the Keplerian orbital frequency and f_{LT} is the point particle LT precession frequency at r (ID11). The bending wave
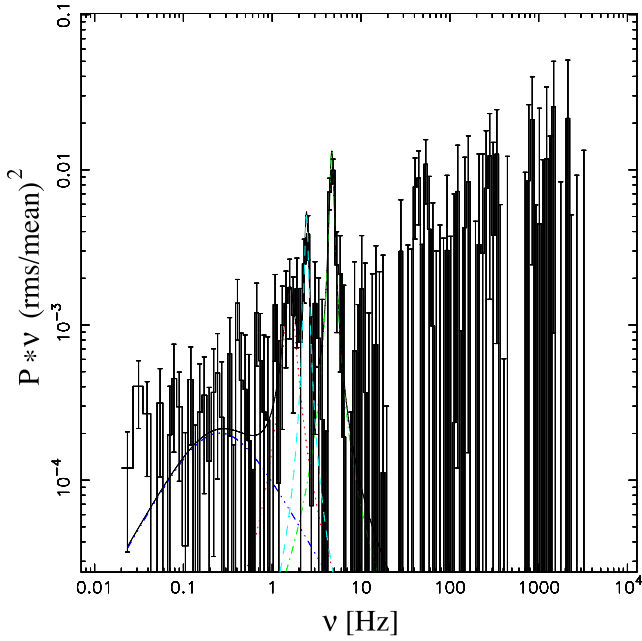
Figure 6. Lorentzian fit of observation 7 showing a type-B QPO.
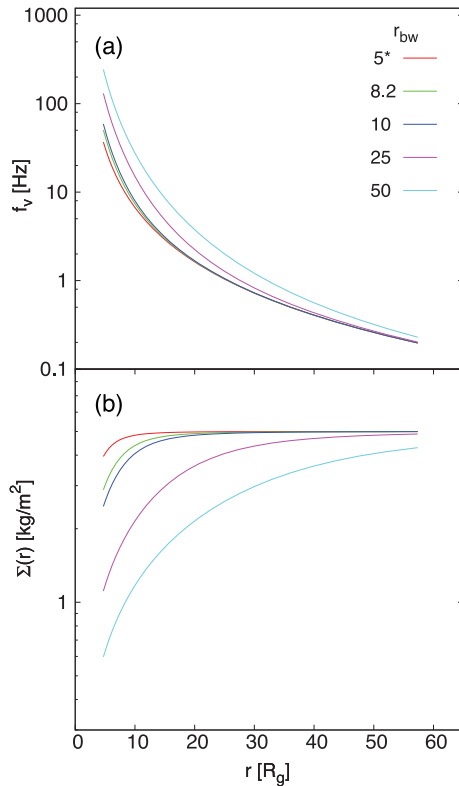

Figure 7. Viscous frequency (a) and surface density profile (b) versus inner flow radius computed varying r_{bw} (Fig. 8b).

radius carries information about the shape of the inner flow because it is dependent on the scaleheight factor of the flow, h/r:

$$r_{bw} = 3(h/r)^{-4/5} a_*^{2/5}, \tag{3}$$

where a_* is the dimensionless spin parameter.

If the mass is conserved on long time-scales, the viscous frequency can be expressed as (Frank, King & Raine 2002; ID12):

$$\nu_{visc}(r) = \frac{\dot{M}_0}{2\pi R^2 \Sigma(r)}. \tag{4}$$

PROPFLUC assumes that the power spectrum of mass accretion rate fluctuations generated at r is a zero-centred Lorentzian cutting off at the viscous frequency. The model splits the flow up into rings and assumes that a constant fractional variability, F_{var}, is generated per decade in radius. The resolution of the model is set by the number of rings per decade in radial extent, N_{dec}; i.e. the interval between $r = 10$ and 100 is split into N_{dec} rings. Consequently, the fractional variability in the mass accretion rate, $\dot{M}(r, t)$, at each ring is $F_{var}/\sqrt{N_{dec}}$, so that N_{dec} of these time series multiplied together has a fractional variability F_{var}. The emitted luminosity from a ring at r_n is then assumed to be $\propto r_n^{2-\gamma} \Sigma(r_n)\dot{M}(r_n, t)$, where the emissivity index $\gamma > 2$ is a model parameter, and the total emitted luminosity is simply the sum of the contributions from each ring. Thus, the low-frequency break in the power spectrum corresponds roughly to $\nu_{visc}(r_o)$ (Churazov et al. 2001; Ingram & Done 2010). The high-frequency break, however, does not correspond to $\nu_{visc}(r_i)$ because interference between radiation from different rings in the flow has a significant influence on the shape of the broad-band noise at high frequencies (ID11; IK13). The emissivity index also clearly affects the shape of the high-frequency noise: increasing γ increases the amount of high-frequency noise in the power spectrum.

4.2 Exploration of model parameters

To better understand the relation between the phenomenological parameters derived from Lorentzian power spectral fit characteristics and the physical parameters of PROPFLUC, and to provide guidance in fitting this model to observed power spectra whose rough characteristics are known, we compute model power spectra with a Nyquist frequency of 128 Hz and vary one by one the main parameters. We fix the BH mass ($10 M_\odot$), the dimensionless spin parameter ($a_* = 0.5$), the inner radius ($r_i = 4.5 R_g$, so that $r_i > r_{ISCO}$), the bending wave radius ($r_{bw} = 8.2$, so that $h/r \sim 0.2$), and the emissivity index ($\gamma = 4.0$). We use a resolution $N_{dec} = 25$ and include a QPO with fixed width and rms. The results of the calculations are shown in Fig. 8. Every plot specifies the parameter values, the asterisk in each panel denotes the value of that parameter used for all the other computations.

Fig. 8(a) shows that the centroid frequency of the broad-band component (hereafter ν_b) decreases as Σ_0 increases, while the centroid frequency of the QPO (hereafter ν_{qpo}) does not change. This can be understood from equations (2) and (4). Equation (4) shows that increasing Σ_0 decreases $\nu_{visc}(r_0) \approx \nu_b$ but, since both integrals in equation (2) contain the surface density, the constant Σ_0 cancels in the calculation of ν_{QPO}. In contrast, the *shape* of the surface density profile affects both the broad-band noise and ν_{qpo}. Equation (2) shows that the precession frequency of the entire flow is a surface density weighted average of $\nu_{LT}(r)$ (the precession frequency of a test mass a distance r from the BH). Therefore, increasing the surface density at large r slows down precession and increasing the surface density at small r speeds up precession. Equation (4) and Figs 7(a) and (b) show that increasing the surface density in any region decreases the viscous frequency in that region and increasing the *gradient* of $\Sigma(r)$ increases the *range* of frequencies at which the broad-band noise contains significant power.

Fig. 8(b) shows that ν_{qpo} decreases with increasing r_{bw}. This is because r_{bw} governs where in the flow the surface density starts
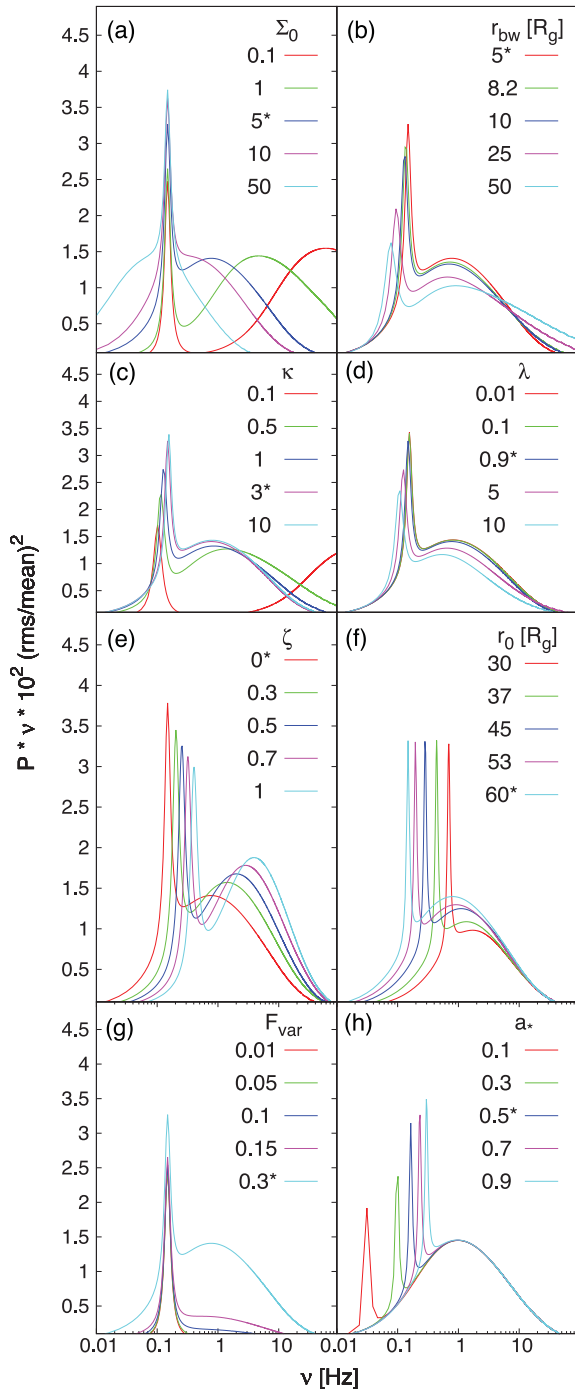
Figure 8. Power spectra computed varying each of the main physical parameters of the model in turn as indicated. Asterisk indicates value of each parameter for all other computations.

regions of the flow (see IK13). Similar considerations are also valid for Figs 8(c)–(e).

Fig. 8(f) shows $\nu_{\rm qpo}$ increasing as $r_{\rm o}$ decreases, roughly following the trend $\nu_{\rm qpo} \propto r_{\rm o}^{-C}$, where C is a positive constant ($C \sim 2.2$ for the fiducial model parameters). This can be understood if we assume a constant surface density profile (i.e. $\zeta = 0$ and $r_{\rm bw}$ is small), and use the weak field approximation for LT precession, $\nu_{\rm LT}(r) \propto r^{-3}$, to obtain a simplified version of equation 2 in Ingram et al. (2009):

$$\nu_{\rm qpo} = \frac{5a_*}{\pi} \frac{[1 - (r_{\rm i}/r_{\rm o})^{1/2}]}{r_{\rm o}^{5/2} r_{\rm i}^{1/2} [1 - (r_{\rm i}/r_{\rm o})^{5/2}]} \frac{c}{R_{\rm g}}. \tag{5}$$

We see that, for $r_{\rm i}/r_{\rm o} \ll 1$, the $r_{\rm o}$ dependence of $\nu_{\rm qpo}$ reduces to $\nu_{\rm qpo}(r_{\rm o}) \propto {\sim} r_{\rm o}^{-5/2} \sim r_{\rm o}^{-2.2}$. We also see from this equation that increasing a_* increases the QPO frequency, as demonstrated in Fig. 8(h). Thus, the parameters which most affect the QPO frequency are $r_{\rm o}$ ($\sim$quadratic) and a_* (linear).

4.3 The fit

As described in Section 4.1, the model is based on the inner accretion flow variability. For this reason, in order to avoid contamination from the disc, the best data choice for fitting would be observations in the high-energy band ($\sim$10–20 keV), as mentioned in ID11. Because of the low count rate, we considered a wide 2.87–20.20 keV band. The model assumes that all the variability is generated in the hot flow, so formally, in this scenario, the only effect of the disc is to suppress the variability amplitudes at lower energies by dilution. Of course, the possibility that the variability is generated in the disc and then propagates towards the inner flow affecting its emission, cannot be excluded, but for our first explorative fit we just considered the simple scenario described above. We note that, using the spectral model *Tbabs * smedge * (discbb + nthComp + gauss)* (Mitsuda et al. 1984; Zdziarski, Johnson & Magdziarz 1996; Życki, Done & Smith 1999; Wilms, Allen & McCray 2000), we find that the disc contribution to the flux in band 1 increases from $\sim$38 per cent in observation 1 to $\sim$61 per cent in observation 7 (it contributes significantly less in the other bands). Since the rms in band 1 decreases from $\sim$33 to $\sim$5 per cent for observations 1–7, our assumption that the disc is stable implies that the fractional rms of the flow in this band is $\sim$53 to $\sim$13 per cent for observations 1–7 respectively, which is reasonable.

Since PROPFLUC is not intended to explain the SIMS, we only fit the first five observations and leave a discussion of qualitative interpretation of observations 6 and 7 to Section 5, in the absence of statistically acceptable fits. We fitted logarithmically binned data points in the frequency range 1/128–128 Hz, using the same resolution for data and model. We used $N_{\rm dec} = 15$ for all the fits. Compared to power spectra computed using higher resolution (see Section 4.2), we did not observe any significant difference in χ^2. The difference produced by a larger number of rings is appreciable only in the higher frequency region of the power spectra, where our data error bars are large. We combined the QPO with the broadband variability by multiplication instead of addition mode (the total flux is the product between the two types of variability instead of their sum, see IK13). Although our observations do not allow us to differentiate between the multiplicative and the additive mode, the multiplicative mode is based on the more physically realistic scenario that the precession modulates the emission. Because of the inner flow precession, the brightest part of the inner flow moves in and out of the observer's line of sight and angles to the line of sight vary, causing variations in the projected area (IK13).
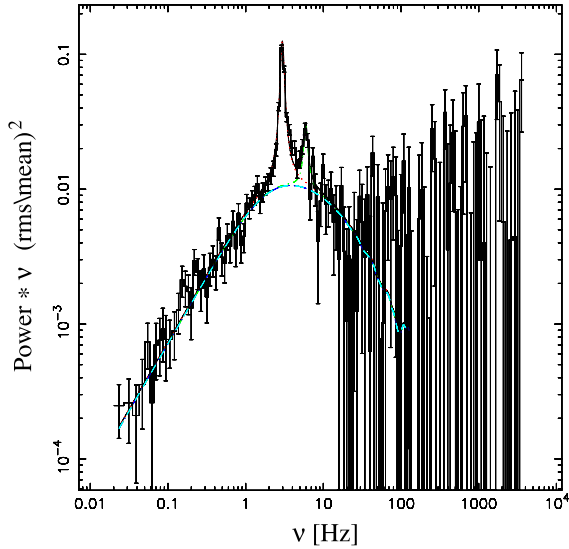
to drop off (see Fig. 7b), and so increasing it weights the surface density towards the outer regions of the flow. Since, as demonstrated in Fig. 7, increasing $r_{\rm bw}$ slightly reduces the average surface density, this slightly increases the viscous frequency at the inner and outer rings in the flow, $\nu_{\rm visc}(r_{\rm i})$ and $\nu_{\rm visc}(r_{\rm o})$. This causes $\nu_{\rm b}$ to increase by a small amount (which is difficult to see in Fig. 8(b) because of the QPO), and its affect on the high-frequency power is complicated by the emissivity and interference between radiation from different

Figure 9. PROPFLUC fit of the third power spectrum.

For all the fits, we fixed the parameters ζ, λ, κ, the bending wave radius r_{bw}, the emissivity γ, the mass M, and the dimensionless spin parameter of the BH a_*. The free parameters are Σ_0, the truncation radius r_{o}, the fractional variability F_{var}, the fundamental QPO width $\Delta\nu$, and the rms of the fundamental and harmonic QPOs.

Fig. 9 shows the PROPFLUC fit of the third observation, Table 2 shows the best-fitting parameters, the main QPO frequency ν_{QPO}, and the reduced χ_ν^2 for each of the five observations considered, and Fig. 10 shows the evolution of the physical parameters with time.

All parameter values show a clear trend. Σ_0 increases from ~3.5 to ~13 continuously. In the same way, the truncation radius decreases from $\sim24\,R_{\mathrm{g}}$ to $\sim10\,R_{\mathrm{g}}$, indicating an average truncation radius recession speed of about $2\,\mathrm{km\,h^{-1}}$. The fractional variability increases from ~18 to ~23 per cent in the first three observations and shows no significant change beyond. The fundamental QPO width increases continuously with time while its rms decreases from ~18 to ~10 per cent.

5 DISCUSSION

As described by Stiele et al. (2012), the source follows the usual behaviour of BHBs. Using the state classification described in Belloni (2010), the source either is in the HS or in the HIMS during the first five observations. Between observations 5 and 7 we observe rms dropping off (from ~18 to ~7 per cent) simultaneously to the detection of radio emission (Miller-Jones et al. 2011), and in observation 7, we identify a significant (4.7σ, single trial) type-B QPO in the 2.87–20.20 keV energy band. This shows that the source entered the SIMS between observations 5 and 7, a conclusion previously considered by Stiele et al. (2012), who however did not report the QPO in observation 7.

We used the PROFLUC model (ID11; ID12; IK13) for fitting the power spectra of the first five observations in the 2.87–20.20 keV band. As described in Section 1, the model assumes that the variability generated by each region of the inner flow peaks at the local viscous time-scale. This is contrary to results of General Relativistic Magneto-Hydrodynamic simulations, which display variability peaking approximately at the local *orbital* time-scale (Armitage & Reynolds 2003; Dexter & Fragile 2011). These simulations, however, disagree with observations since BHBs display a high-frequency break in their power spectra at $\nu \lesssim 10$ Hz, whereas simulations assuming a $10\,\mathrm{M_\odot}$ BH exhibit variability up to a high-frequency break of ~100 Hz, $\sim1/3$ the orbital frequency at $5R_{\mathrm{g}}$ (e.g., fig. 10 of Dexter & Fragile 2011). The same discrepancy with simulations is seen for active galactic nuclei. For example, the power spectrum of the Seyfert 1 galaxy NGC 4051 displays a break at $\sim8 \times 10^{-4}$ Hz (Vaughan et al. 2011), whereas the orbital frequency at $5R_{\mathrm{g}}$ is $\sim1.7 \times 10^{-2}$ Hz (assuming a BH mass of $\sim1.7 \times 10^6\,\mathrm{M_\odot}$). While it is clearly important that this inconsistency is addressed, we note that assuming the characteristic variability time-scale to be orbital rather than viscous would require an inner flow radius of $r_{\mathrm{i}} \sim 75R_{\mathrm{g}}$ in order to fit the observed power spectra in this paper. This strongly implies that considering the viscous time-scale is more appropriate for BHs, even in light of evidence that pulsars show variability on the orbital time-scale (Revnivtsev et al. 2009).

In order to better explore the possibilities of the model, we ran a series of computations varying its physical parameters. The model

Table 2. Best PROPFLUC fit physical parameters for observations 1–5. An $\sim$ symbol indicates that the parameter has been fixed.

| Observations	1	2	3	4	5
Σ_0	$3.47^{+1.12}_{-0.64}$	$4.95^{+0.34}_{-0.89}$	$6.65^{+0.25}_{-0.04}$	$9.90^{+0.94}_{-1.37}$	$13.24^{+2.08}_{-0.56}$
F_{var} (%)	$18.84^{+0.44}_{-1.32}$	$20.73^{+0.79}_{-0.92}$	$22.66^{+0.44}_{-0.60}$	$22.84^{+0.23}_{-0.31}$	$22.97^{+0.36}_{-0.26}$
ζ	0	$\sim$	$\sim$	$\sim$	$\sim$
λ	0.90	$\sim$	$\sim$	$\sim$	$\sim$
κ	3.00	$\sim$	$\sim$	$\sim$	$\sim$
r_{i}	4.50	$\sim$	$\sim$	$\sim$	$\sim$
r_{bw}	8.24	$\sim$	$\sim$	$\sim$	$\sim$
r_{o}	$23.56^{+0.05}_{-0.07}$	$18.59^{+0.01}_{-0.01}$	$14.40^{+0.00}_{-0.00}$	$11.87^{+0.00}_{-0.01}$	$10.32^{+0.01}_{-0.01}$
$\Delta\nu_{\mathrm{qpo}}(10^{-2})$	$9.97^{+1.17}_{-2.01}$	$11.44^{+0.61}_{-1.64}$	$17.75^{+1.23}_{-0.98}$	$19.55^{+3.88}_{-4.86}$	$37.76^{+4.60}_{-2.84}$
σ_{qpo} (%)	$17.34^{+1.24}_{-1.24}$	$14.83^{+0.08}_{-0.18}$	$14.71^{+0.08}_{-0.09}$	$12.99^{+0.50}_{-0.57}$	$10.61^{+0.51}_{-0.46}$
σ_{2apo} (%)	0.	0.	$5.88^{+0.27}_{-0.22}$	$5.04^{+0.82}_{-0.12}$	$4.71^{+0.78}_{-0.84}$
γ	4.0	$\sim$	$\sim$	$\sim$	$\sim$
$M(\mathrm{M_\odot})$	10.0	$\sim$	$\sim$	$\sim$	$\sim$
a	0.5	$\sim$	$\sim$	$\sim$	$\sim$
ν_{qpo} (Hz)	1.06	1.75	2.97	4.38	5.78
χ_ν^2	0.90	0.91	1.25	0.89	0.99
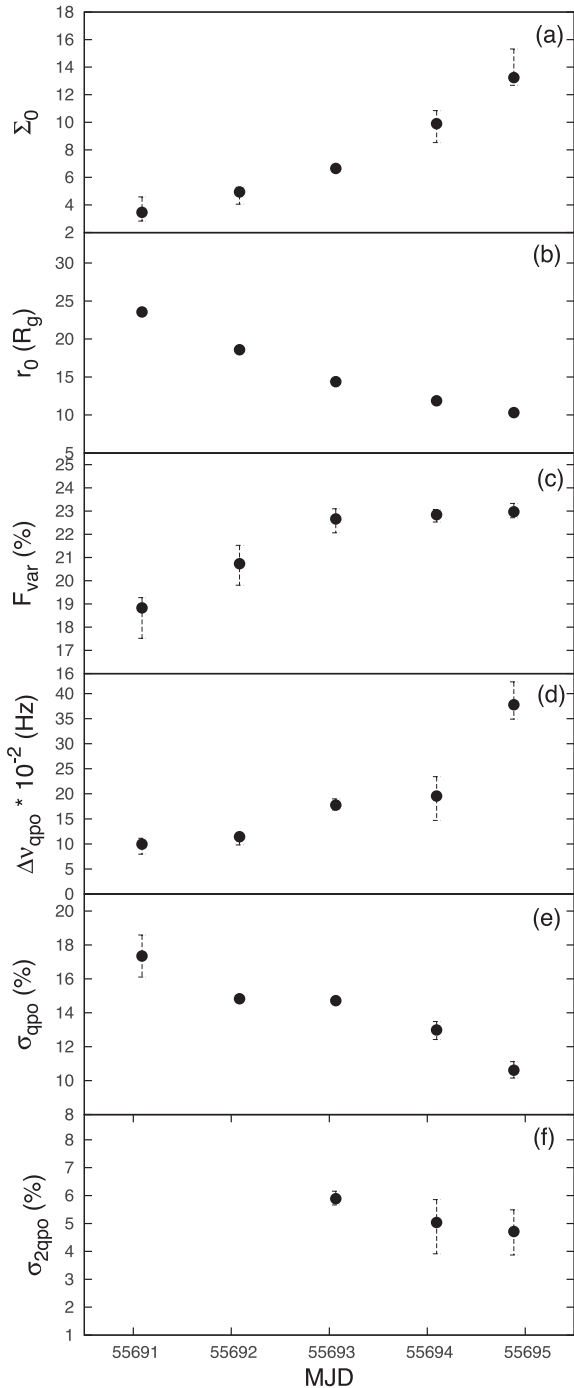
Figure 10. PROFLUC best-fitting parameters versus time. All the points were plotted with 1σ error bars.

parameter mainly affecting QPO frequency is the truncation radius r_o, which sets the physical dimension of the precessing inner flow, responsible for the QPO generation. As can be seen in Fig. 8, most other parameters (but not Σ_0 and F_{var}) also affect the QPO frequency. Every parameter affects the broad-band noise in a characteristic way. For example, varying the bending wave radius r_{bw} we observe evident correlated variations in peak frequency and slope of the high-frequency tail of the broad-band component, varying ζ has almost no effect on the high-frequency tail, but clearly changes its width and peak frequency, Σ_0 variations affect only the peak frequency. Variations in BH spin a_* have no effect at all on the

broad-band component. It is clear that in order to constrain all physical parameters of the model, very good counting statistics are needed to clearly define the precise shape of the broad-band noise.

In our fits, we fixed λ, ζ, κ, r_{bw}, the emission coefficient γ, BH mass M, and spin a_*. Fixing λ, ζ, κ, and r_{bw} implies fixing the surface density profile throughout the rising phase of the outburst. ID12 noticed that an evolution of r_{bw} is expected when the truncation radius decreases, because when the inner flow is illuminated by an increasing number of disc photons, its electron temperature drops, and hence its scaleheight factor, h/r, collapses. In our fit, we fixed the bending wave radius because our spectra are too noisy above 10 Hz to measure it independently, so we are not able to eliminate the degeneracy between r_o and r_{bw} in determining the QPO frequency. For this reason, we caution that the fit results in this work were obtained fixing the density profile of the inner flow (except for r_o), so that they must be interpreted with care.

The QPO frequency increase over observations 1–5 corresponds to an r_o decrease from $\sim$24 to $\sim$10 R_g. From spectral analysis, Stiele et al. (2012) report a constant truncation radius ($r_o \sim$ 20–22 km) throughout the whole outburst without specifying uncertainties. As described before, the PROFLUC physical parameter mainly affecting the QPO frequency is r_o, so that, in order to fit QPOs during the rising phase of the outburst, the truncation radius has to vary during this phase. Because of the data quality, *RXTE* spectral range, and the limitations of the model used by Stiele et al. (2012) (see Merloni, Fabian & Ross 2001), the spectral estimation of the inner radius is of limited use in the comparison with the PROFLUC results.

The surface density normalization constant Σ_0 increases from $\sim$3.5 to $\sim$13.2. For a given annulus in the inner flow, Σ_0 is proportional to surface density divided by mass accretion rate (equation 1). During the rising phase of the outburst, the mass accretion rate increases with time, so the Σ_0 increase means that the surface density increases faster than the mass accretion rate, i.e. matter is accumulating in the flow during this phase of the outburst. This is consistent with the results of ID12 on XTE J1550-564.

The fractional variability F_{var} shows a linear increasing trend in the first three observations and holds almost stable ($\sim$23 per cent) in the other observations. The fractional variability does not give us any detailed information about the physical mechanisms producing the variability, but it quantifies the turbulent nature of the accreting material per radial decade. ID12 show that F_{var} increases continuously decreasing truncation radius, but we do not observe the same trend over all the observations, possibly because in our fit we fixed the bending wave radius.

As described, timing properties change in observations 6 and 7, compared to observations 1–5, with simultaneous radio emission. The changes are more abrupt at higher photon energies (Fig. 3). The rms decreases from $\sim$18 to $\sim$7 per cent and L_{LF} frequency decreases as well, breaking the monotonically increasing trend of the first five observations. Observations 6 and 7 also show a prominent low-frequency broad-band component (L_b^-) that is not understandable in terms of the two-component power spectra produced by PROFLUC, which is the reason why we applied PROFLUC only to the first five observations. Belloni et al. (1997) consider emptying and replenishing cycles of the inner accretion disc, caused by viscous thermal instability, to explain variability on time-scale of tens of minutes in GRS 1915+105. Feroci et al. (1999) suggest material ejection to explain both spectral and timing properties of this same source, also in view of the correlation between the innermost disc temperature and the QPO frequency observed by Muno, Morgan & Remillard (1999). Similarly, assuming the truncation radius reaches its smallest value at maximum luminosity (and so maximum
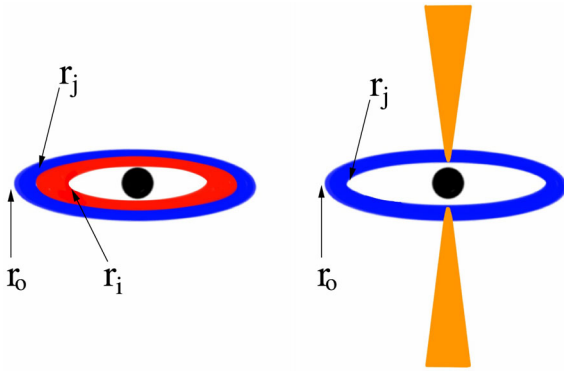
Figure 11. Schematic representation of the transition between HS (a) and SIMS (b).

accretion rate), the ν_{QPO} decrease observed in our data can be explained by the depletion of inner flow material between r_i and a certain radius r_j ($r_o > r_j > r_i$) simultaneously to the radio emission. This scenario is shown schematically in Fig. 11. This depletion can be caused by either ejection or increased accretion between r_i and r_j. As a consequence, the surface density between r_i and r_j drops off, so that the high frequencies (corresponding to smaller radii) contribute less to the QPO frequency (equation 2) and F_{var} (so the noise level) decreases.

The low-frequency broad-band component L_b^- might be explained in this scenario as the result of mass accretion rate fluctuations propagating from the disc towards the inner flow.

6 CONCLUSIONS

We analysed the evolution of MAXI J1543-564 during its 2011 outburst identifying the transition between LHS/HIMS and SIMS, occurring between observations 5 and 6. Analysing the source in different energy bands, we found that in this transition changes in rms are more evident at higher photon energy. Using the mass accretion rate fluctuation/precessing flow model PROPFLUC, we provided a physical interpretation of the first five observations in terms of truncation radius, fractional variability, mass accretion rate, and surface density evolution. We suggest that the source behaviour in observations 6 and 7, and so the transition between LHS and SIMS, might be caused by mass depletion in the innermost part of the accretion flow due to ejection and/or enhanced accretion associated with the simultaneous radio emission. This physical scenario is consistent with our timing analysis in different energy bands.

ACKNOWLEDGEMENTS

REFERENCES

Arévalo P., Uttley P., 2006, MNRAS, 367, 801
Armitage P. J., Reynolds C. S., 2003, MNRAS, 341, 1041
Belloni T. M., 2010, in Belloni T., ed., Lecture Notes in Physics, Vol. 794, The Jet Paradigm. Springer-Verlag, Berlin, p. 53
Belloni T., Mendez M., King A. R., van der Klis M., van Paradijs J., 1997, ApJ, 488, L109
Belloni T., Psaltis D., van der Klis M., 2002, ApJ, 572, 392
Belloni T., Homan J., Casella P., van der Klis M., Nespoli E., Lewin W. H. G., Miller J. M., Méndez M., 2005, A&A, 440, 207
Casella P., Belloni T., Stella L., 2005, ApJ, 629, 403
Churazov E., Gilfanov M., Revnivtsev M., 2001, MNRAS, 321, 759
Dexter J., Fragile P. C., 2011, ApJ, 730, 36
Done C., Gierliński M., Kubota A., 2007, A&AR, 15, 1
Esin A. A., McClintock J. E., Narayan R., 1997, ApJ, 489, 865
Fender R. P., Belloni T. M., Gallo E., 2004, MNRAS, 355, 1105
Fender R., Belloni T., Gallo E., 2005, Ap&SS, 300, 1
Feroci M., Matt G., Pooley G., Costa E., Tavani M., Belloni T., 1999, A&A, 351, 985
Fragile P. C., Blaes O. M., Anninos P., Salmonson J. D., 2007, ApJ, 668, 417
Frank J., King A., Raine D. J., 2002, Accretion Power in Astrophysics. Cambridge Univ. Press, Cambridge
Gilfanov M., 2010, in Belloni T., ed., Lecture Notes in Physics, Vol. 794, The Jet Paradigm. Springer-Verlag, Berlin, p. 17
Homan J., Wijnands R., van der Klis M., Belloni T., van Paradijs J., Klein-Wolt M., Fender R., Méndez M., 2001, ApJS, 132, 377
Ingram A., Done C., 2010, MNRAS, 405, 2447
Ingram A., Done C., 2011, MNRAS, 415, 2323 (ID11)
Ingram A., Done C., 2012, MNRAS, 419, 2369 (ID12)
Ingram A., van der Klis M., 2013, MNRAS, 434, 1476 (IK13)
Ingram A., Done C., Fragile P. C., 2009, MNRAS, 397, L101
Jahoda K., Swank J. H., Giles A. B., Stark M. J., Strohmayer T., Zhang W., Morgan E. H., 1996, Proc. SPIE, 2808, 59
Klein Wolt M., 2004, PhD thesis, Universiteit van Amsterdam
Liu S., Melia F., 2002, ApJ, 573, L23
Lubow S. H., Ogilvie G. I., Pringle J. E., 2002, MNRAS, 337, 706
Lyubarskii Y. E., 1997, MNRAS, 292, 679
Matsuoka M. et al., 2009, PASJ, 61, 999
Merloni A., Fabian A. C., Ross R. R., 2001, in White N. E., Malaguti G., Palumbo G. G. C., eds, AIP Conf. Proc. Vol. 599, X-ray Astronomy: Stellar Endpoints, AGN, and the Diffuse X-ray Background. Am. Inst. Phys., New York, p. 770
Miller-Jones J. C. A., Tzioumis A. K., Jonker P. G. et al., 2011, Astron. Telegram, 3364, 1
Mitsuda K. et al., 1984, PASJ, 36, 741
Muno M. P., Morgan E. H., Remillard R. A., 1999, ApJ, 527, 321
Negoro H. et al., 2011, Astron. Telegram, 3330, 1
Psaltis D., Belloni T., van der Klis M., 1999, ApJ, 520, 262
Remillard R. A., McClintock J. E., 2006, ARA&A, 44, 49
Remillard R. A., Muno M. P., McClintock J. E., Orosz J. A., 2002, ApJ, 580, 1030
Revnivtsev M., Churazov E., Postnov K., Tsygankov S., 2009, A&A, 507, 1211
Shakura N. I., Sunyaev R. A., 1973, A&A, 24, 337
Stiele H., Muñoz-Darias T., Motta S., Belloni T. M., 2012, MNRAS, 422, 679
Sunyaev R. A., Truemper J., 1979, Nature, 279, 506
Thorne K. S., Price R. H., 1975, ApJ, 195, L101
Uttley P., McHardy I. M., 2001, MNRAS, 323, L26
Uttley P., McHardy I. M., Vaughan S., 2005, MNRAS, 359, 345
Vaughan S., Uttley P., Pounds K. A., Nandra K., Strohmayer T. E., 2011, MNRAS, 413, 2489
Wijnands R., van der Klis M., 1998, ApJ, 507, L63
Wijnands R., Homan J., van der Klis M., 1999, ApJ, 526, L33
Wilms J., Allen A., McCray R., 2000, ApJ, 542, 914
Zdziarski A. A., Johnson W. N., Magdziarz P., 1996, MNRAS, 283, 193
Zhang W., Jahoda K., Swank J. H., Morgan E. H., Giles A. B., 1995, ApJ, 449, 930
Życki P. T., Done C., Smith D. A., 1999, MNRAS, 309, 561

This paper has been typeset from a TeX/LaTeX file prepared by the author.